Nanoscale

PAPER

View Article Online
View Journal | View Issue

Cite this: *Nanoscale*, 2018, **10**, 22520

Structural characterization of heterogeneous RhAu nanoparticles from a microwave-assisted synthesis†

Zhiyao Duan,‡[a] Janis Timoshenko, ‡[b] Pranaw Kunal,[c] Stephen D. House, [d] Haqin Wan,[c] Karalee Jarvis,[e] Cecile Bonifacio,[d] Judith C. Yang,[d,f] Richard M. Crooks, [e,g] Anatoly I. Frenkel, [h] Simon M. Humphrey [e,i] and Graeme Henkelman *[e,j]

A microwave assisted method was used to synthesize RhAu nanoparticles (NPs). Characterization, based upon transmission electron microscopy (TEM), energy dispersive spectroscopy, and powder X-ray diffraction, provided the evidence of monomodal alloy NPs with a mean size distribution between 3 and 5 nm, depending upon the composition. Extended X-ray adsorption fine-structure spectroscopy (EXAFS) also showed evidence of alloying, but the coordination numbers of Rh and Au indicated significant segregation between the metals. More problematic were the low coordination numbers for Rh; values of *ca.* 9 indicate NPs smaller than 2 nm, significantly smaller than those observed with TEM. Additionally, no single-particle structural models were able to reproduce the experimental EXAFS data. Resolution of this discrepancy was achieved with high resolution aberration corrected scanning TEM imaging which showed the presence of ultra-small (<2 nm) pure Rh clusters and larger (~3–5 nm) segregated particles with Au-rich cores and Rh-decorated shells. A heterogeneous model with a mixture of ultrasmall pure Rh clusters and larger segregated Rh/Au NPs was able to explain the experimental measurements of the NPs over the range of compositions measured. The combination of density functional theory, EXAFS, and TEM allowed us to quantify the heterogeneity in the RhAu NPs. It was only through this combination of theoretical and experimental techniques that resulted in a bimodal distribution of particle sizes that was able to explain all of the experimental characterization data.

Received 14th June 2018,
Accepted 1st November 2018

DOI: 10.1039/c8nr04866e

rsc.li/nanoscale

1. Introduction

Metal nanoparticles (MNPs) are important for catalysis both because they have a high surface area to volume ratio and because the catalytic properties of nanosized noble metals can be significantly different from bulk materials.[1] A tremendous amount of research on catalysis focuses on MNPs containing more than one component.[2–4] It has been shown, for example, that the use of two or more metals can tune the catalytic properties of MNPs and even result in properties that are significantly different from those of the individual components.[5,6] Correlations between the structure and function of alloy metal MNPs have been understood in terms of strain in the surface layer, electronic or ligand interactions between components, and the presence of under-coordinated sites and specific ensembles on the MNP surface. Notably, by exploiting properties unique to the nanoscale, unusual solid-solution alloy MNPs can be accessed between noble metals that are immiscible (or metastable) in the bulk, and therefore previously not studied. Here, we consider one such case involving nanosized RhAu mixtures. Rh and Au are immiscible in the bulk over the

---

[a] Department of Chemistry and the Institute for Computational Engineering and Sciences, The University of Texas at Austin, Austin, TX 78712-0165, USA
[b] Department of Materials Science and Chemical Engineering, Stony Brook University, Stony Brook, NY11794-2275, USA
[c] Department of Chemistry, The University of Texas at Austin, Austin, TX 78712-0165, USA
[d] Department of Chemical and Petroleum Engineering, The University of Pittsburgh, Pittsburgh, PA 15261, USA
[e] Texas Materials Institute, The University of Texas at Austin, Austin, TX 78712-0165, USA
[f] Department of Physics and Astronomy, The University of Pittsburgh, Pittsburgh, PA 15261, USA
[g] Department of Chemistry, The University of Texas at Austin, Austin, TX 78712-0165, USA. E-mail: crooks@cm.utexas.edu
[h] Department of Materials Science and Chemical Engineering, Stony Brook University, Stony Brook, NY, 11794-2275, USA. E-mail: anatoly.frenkel@stonybrook.edu
[i] Department of Chemistry, The University of Texas at Austin, Austin, TX 78712-0165, USA. E-mail: smh@cm.utexas.edu
[j] Department of Chemistry and the Institute for Computational Engineering and Sciences, The University of Texas at Austin, Austin, TX 78712-0165, USA. E-mail: henkelman@utexas.edu; Fax: +1512 471 8696; Tel: +1 512 471 4170

† Electronic supplementary information (ESI) available. See DOI: 10.1039/C8NR04866E

‡ These authors contributed equally to the paper.

entire composition range, preferring to undergo segregation from liquid co-melts below 2158 K. The RhAuNPs used in this study were prepared using a microwave assisted method reported recently,[7] and then a range of characterization and modeling techniques were used to try to understand the structure of the resulting RhAuNPs.

RhAuNPs have been prepared previously both in our group[7] and by others using solution-phase approaches.[8] Piccolo *et al.* reported a significant segregation of Rh and Au in the alloy particles.[8] In our previous studies, using the same microwave synthesis that is used here, we found that a random alloy model was in agreement with X-ray diffraction data and could be used to understand the enhanced activity of these species when supported on SiO_2, in the vapor-phase hydrogenation of cyclohexene.[7] Here, we aim to gain a deeper understanding of the detailed structures of these particles as a step towards a better understanding of how they function as catalysts. As we will show, the synthesized RhAu particles are clearly heterogeneous in both size and composition, which poses formidable challenges for ensemble-averaging characterization methods, including X-ray absorption fine structure (XAFS), and imaging methods, including TEM. Fortunately, these two types of methods can provide complementary structural information; thus, it is increasingly common to utilize a combination of methods to accurately describe the structural complexities that are inherent in these complex nanoscale systems.[9] In this study, we employ a similar philosophy to analyze the structure of the RhAu NPs in terms of size, composition, and elemental distribution. We also extend the structural characterization to fully atomic models by reproducing EXAFS spectra with atomistic simulations. Perhaps the most interesting aspect of this work is that the initial attempts at characterization misled us, and only through the use of a range of characterization techniques combined with modeling are we finally able to present a structural model which is in complete agreement with all the data. To highlight this aspect of the work, the results are described as they were obtained.

2. Results and discussion

2.1. Synthesis

Rh_xAu_{1-x}NPs were synthesized using a microwave-assisted technique. All microwave assisted reactions were carried out inside a custom-designed microwave cavity as reported previously.[7] Briefly, Rh(III) and Au(III) metal salts were dissolved in ethylene glycol with a nominal molar ratio based on the desired NP composition. The metal salts were directly co-injected at a controlled rate into a stirred ethlyne glycol (EG) solution kept at 150 °C, containing poly(vinylpyrrolidone) and $NaBH_4$. After 30 minutes, the mixture was quenched in ice water and the resulting NPs were purified in acetone.

A set of RhAuNPs with nominal compositions, 0.3 : 0.7, 0.5 : 0.5, 0.7 : 0.3, and 0.9 : 0.1, as determined by the ratio of metal precursors. The Rh-rich samples were the focus of our characterization because this range of compositions was previously found to be most active for hydrogenation reactions.[7] The actual composition of the NPs was measured independently using ICP-OES, XAS, and STEM-EDS; the measured Rh : Au ratios are shown in Table 1. The ICP-OES and STEM-EDS analyses showed somewhat higher Au compositions as compared to the nominal (target) compositions, while the XAS showed higher Rh ratios.

Table 1 Elemental composition values of Rh_xAu_{1-x}NPs as determined by different characterization techniques

Sample	EDS	XAS	ICP-OES
$Rh_{0.3}Au_{0.7}$	0.29 : 0.71	—	0.18 : 0.82
$Rh_{0.5}Au_{0.5}$	0.56 : 0.44	0.62 : 0.38	0.41 : 0.59
$Rh_{0.7}Au_{0.3}$	0.70 : 0.30	0.84 : 0.16	0.55 : 0.45
$Rh_{0.9}Au_{0.1}$	0.97 : 0.03	0.87 : 0.13	0.84 : 0.16

Powder X-ray diffraction (PXRD, Fig. 1a) was used to measure the lattice spacing of the NPs. The fact that intermediate compositions of Rh_xAu_{1-x}NPs show continuous peak shifts between those of the component metals was a factor that led us to believe that Rh and Au were randomly alloyed/well mixed in the NPs.[7] A plot of the lattice constant as a function of composition, derived using the Scherrer equation, is shown in Fig. 1b. A homogeneous alloy would follow Vegard's law (dashed line). While our NPs are clearly not perfect alloys, the continuous lattice constant shift is the evidence for alloying between Rh and Au.

2.2. TEM characterization

Low-resolution TEM (Fig. 2) shows that the average measured RhAuNP size increases with increasing Au content, ranging

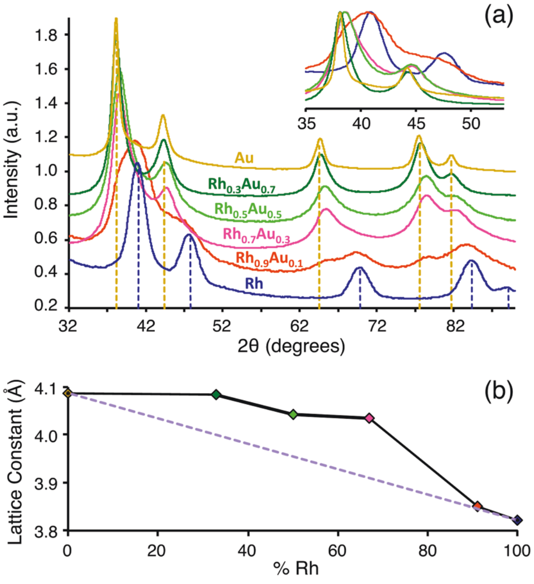

Fig. 1 (a) PXRD data of Rh_xAu_{1-x} alloy NPs. Rh and Au reference peaks are shown as dashed lines in blue and gold, respectively. (b) Variation of lattice constants with the composition of RhAu alloy NPs; the dashed purple line shows the trend with theoretical values calculated using Vegard's law. Different colored points correspond to various compositions obtained using ICP-OES.

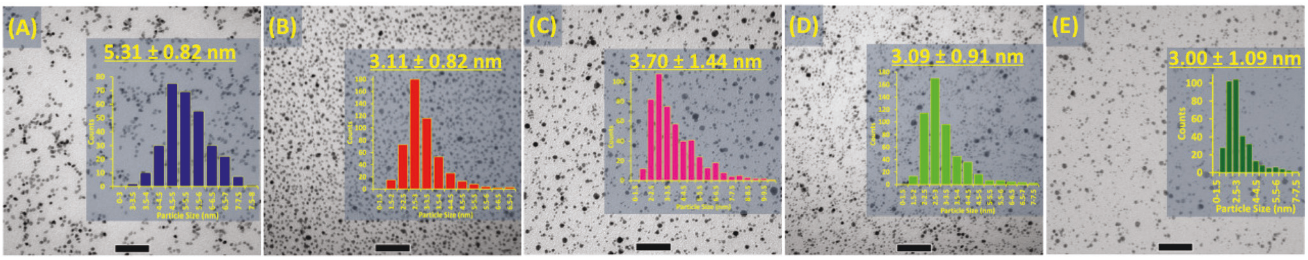

Fig. 2 TEM images and size distributions of NPs: (a) Rh, (b) $Rh_{0.9}Au_{0.1}$, (c) $Rh_{0.7}Au_{0.3}$, (d) $Rh_{0.5}Au_{0.5}$, and (e) $Rh_{0.3}Au_{0.7}$. The black scale bars indicate 50 nm.

between 3–5 nm. The more Au-rich NPs are also more polydisperse. Note that for all NP compositions, the size distributions are monomodal, which we felt should justify the identification of a single NP with a characteristic size and composition.

Our PXRD analysis shows a varying degree of peak broadening for the RhAuNPs. Notably, significant peak broadening is seen for $Rh_{0.9}Au_{0.1}$ NPs, which indicates the presence of small NPs. However, such NPs were not seen in our low-resolution TEM analysis (size distribution graph, Fig. 2). High-resolution STEM was subsequently used, which gave a clear picture of small nanoclusters, as discussed below.

High-resolution TEM images of $Rh_{0.5}Au_{0.5}$NPs in Fig. 3a reveal roughly spherical (cuboctahedral) particles ranging from 2 to 5 nm. The EDS maps in Fig. 3b and c show the co-localization of Au and Rh in these particles. A line scan through a single particle, imaged with high-angle annular dark-field scanning TEM (HAADF-STEM) (Fig. 4), shows that the distribution of Rh and Au is not uniform, with Au favoring the core and Rh favoring the shell in the particles as imaged.

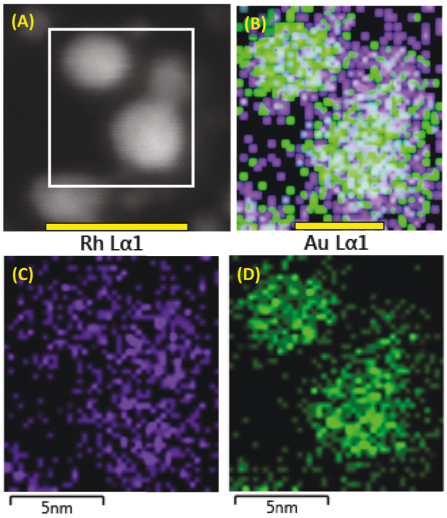

Fig. 3 (a) HAADF-STEM micrograph of $Rh_{0.5}Au_{0.5}$NPs. The scale bar is 10 nm. (b) EDS elemental map showing the overlaid spatial distributions of Au (green) and Rh (purple) in the selected area indicated by the white rectangular box in (a); the scale bar is 5 nm. (c) and (d) show the individual EDS maps of Au and Rh, respectively.

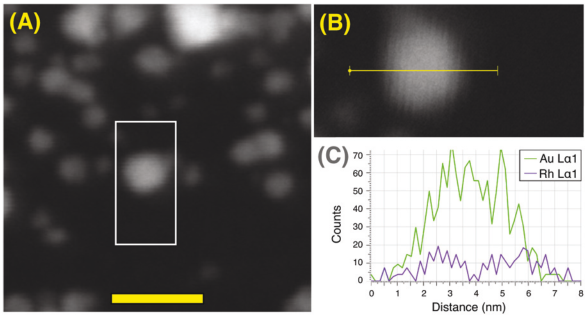

Fig. 4 (a) High-angle annular dark-field (HAADF-STEM) image of $Rh_{0.5}Au_{0.5}$NPs; the scale bar is 10 nm; (b) 2D EDS mapping results of the selected area indicated by the white rectangular box in (a); (c) show an EDS line scan across a single NP.

2.3. XANES analysis

Normalized X-ray adsorption near-edge structures (XANES spectra) for the Au L_3-edge and the Rh K-edge are shown in Fig. 5a and b, respectively. XAS analysis was performed on the $Rh_{0.9}Au_{0.1}$, $Rh_{0.7}Au_{0.3}$, and $Rh_{0.5}Au_{0.5}$ samples. XANES spectra of all samples bear a strong resemblance to that of metallic Rh. Only the XANES spectra for the $Rh_{0.5}Au_{0.5}$NPs show that

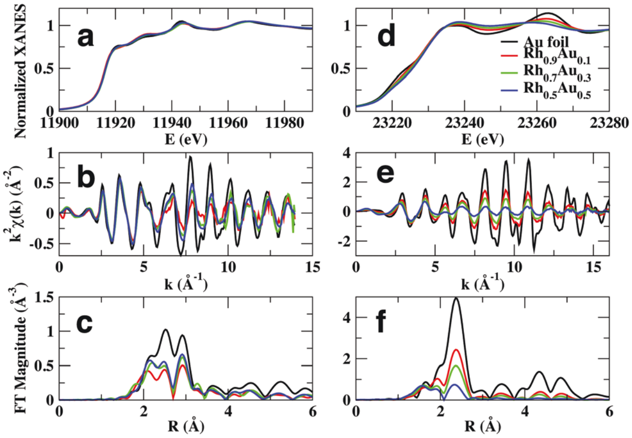

Fig. 5 Au L_3-edge (left column) and Rh K-edge (right column) EXAFS spectra for the Au and Rh foils and for as-prepared RhAu NP samples. Experimental XANES spectra (a, d), EXAFS spectra (b, e), and their Fourier transforms (FT) (c, f) are shown.

the as-prepared sample may be oxidized, as evidenced by the shift of the absorption edge and the features at low interatomic distances in the corresponding EXAFS spectrum, shown in Fig. 5f. When the sample was mildly heated under an atmosphere of H_2 gas, it was noted that the fraction of oxide decreased (as evidenced by the shift of the XANES edge closer to the rest of the samples). The EXAFS results obtained for the as-prepared and H_2-treated sample are very similar, however, suggesting that the influence of the oxide fraction (if any) is minor. Therefore, we discuss only the results obtained for the untreated sample.

The Au L_3-edge XANES data resemble those of Au foil. For the purpose of our structural characterization, it is particularly important to note that even though the majority of atoms in the samples are Rh, the XANES spectra for the Au atoms are close to those of bulk Au, suggesting some segregation of Au atoms.

2.4. EXAFS analysis

The structural parameters obtained from a fit of both the Rh and Au EXAFS data are summarized in Table 2. The experimental and fitted spectra (Fig. S1†) show excellent agreement. The EXAFS-fit structural parameters suggest that Rh and Au atoms are at least partially segregated. For all samples, both the Rh K-edge and Au L_3-edge EXAFS spectra are dominated by monometallic contributions. Even for the Rh-rich samples, the Au–Au coordination number exceeds that for Au–Rh by factors of 2–6. For a random alloy, the ratio of the Au–Au coordination number to the Au–Rh coordination number should be equal to the molar ratio of Au to Rh atoms in the particles.[10] For example, in the $Rh_{0.7}Au_{0.3}$ sample where Rh exceeds Au by more than a factor of two, the Au–Au coordination number should be half that of Au–Rh, and yet it was found to be double. These EXAFS data indicate that a homogeneous alloy is not a good model for the RhAu particles and that there must be Au-rich regions and Rh-rich regions, which enhanced the homometallic coordination numbers.

Nevertheless, the contribution of Au–Rh bonds was important to obtain a good fit to the experimental data, indicating that some fraction of Rh is indeed alloyed with Au. In addition, the Au–Au distance in all samples is about 0.03–0.04 Å smaller than that of bulk Au. For particles of this size (*ca.* 3 nm, according to TEM), there should not be such a large difference in the Au–Au bond length if the particles were pure Au.[11] The observed reduction in interatomic distances can be explained by Au–Rh alloying, because Rh has a smaller lattice constant than Au. Another possibility is that Au–Rh bonding could occur at the interface of segregated Au and Rh domains.

In addition, we found that the total Rh coordination number ($N_{\mathrm{Rh-Rh}}$ + $N_{\mathrm{Rh-Au}}$) is surprisingly small for the $Rh_{0.7}Au_{0.3}$ and $Rh_{0.5}Au_{0.5}$NPs (6.8 and 5.6, respectively). For a model approximating the ensemble by a single representative particle, coordination numbers this low should correspond to particles smaller than 2 nm.

2.5. STEM characterization

The apparent discrepancy between TEM, PXRD, and EXAFS characterization prompted our employment of high-resolution aberration-corrected STEM (AC-STEM) analysis. The aim was to resolve the apparent disagreement between what appeared to be a monomodal distribution of alloy nanoparticles from TEM and PXRD with the largely segregated NPs with oddly low coordination numbers, as indicated by EXAFS that suggested a size inconsistent with the TEM images. Our analysis focused on the 0.5 : 0.5 and 0.9 : 0.1 Rh/Au samples.

Conventional S/TEM imaging was performed using a JEOL JEM 2100F at the Nanoscale Fabrication and Characterization Facility (NFCF) at the University of Pittsburgh and an FEI Talos F200X at the Center for Functional Nanomaterials (CFN) at Brookhaven National Laboratory. Initial measurements indicated sizes of 2.48 ± 0.91 nm and 3.18 ± 0.53 nm for the $Rh_{0.5}Au_{0.5}$ and $Rh_{0.9}Au_{0.1}$ samples, respectively. A wide range of sizes, however, from about 1–8 nm was observed. This analysis is consistent with what we found previously.

An FEI Themis 300 aberration-corrected S/TEM – usage courtesy of FEI – was subsequently employed to achieve the necessary spatial resolution both for imaging and energy-dispersive X-ray spectroscopy (EDS) mapping of the elemental composition. Equipped with a high-brightness gun and Super-X EDS, this microscope enabled single-atom resolution (Fig. 6)

Table 2 Values of structural parameters (Rh–Rh, Rh–Au, Au–Au and Au–Rh coordination numbers *N*, average interatomic distances $\langle R\rangle$, and Debye–Waller factors σ^2) for the first coordination shell of Rh and Au atoms in the NPs obtained from the fits of Au L_3-edge and Rh K-edge EXAFS data. Uncertainties in the last significant digits are given in parentheses

	Rh foil	Au foil	$Rh_{0.9}Au_{0.1}$NPs	$Rh_{0.7}Au_{0.3}$NPs	$Rh_{0.5}Au_{0.5}$NPs
$N_{\mathrm{Rh-Rh}}$	12	—	8.7(4)	6.0(3)	4.6(2)
$N_{\mathrm{Rh-Au}}$	—	—	0.3(1)	0.8(5)	1.0(2)
$N_{\mathrm{Au-Au}}$	—	12	7(1)	8(1)	8.8(3)
$N_{\mathrm{Au-Rh}}$	—	—	2.2(7)	4(2)	1.5(2)
$\langle R\rangle_{\mathrm{Rh-Rh}}$ (Å)	2.682(1)	—	2.680(1)	2.681(1)	2.686(2)
$\langle R\rangle_{\mathrm{Rh-Au}}$ (Å)	—	—	2.74(1)	2.79(2)	2.786(5)
$\langle R\rangle_{\mathrm{Au-Au}}$ (Å)	—	2.861(5)	2.821(5)	2.829(3)	2.833(1)
$\langle R\rangle_{\mathrm{Au-Rh}}$ (Å)	—	—	2.74(1)	2.79(2)	2.786(5)
${\sigma_{\mathrm{Rh-Rh}}}^2$ (10^{-2} Å^2)	0.36(2)	—	0.58(2)	0.61(2)	0.67(5)
${\sigma_{\mathrm{Rh-Au}}}^2$ (10^{-2} Å^2)	—	—	1.0(2)	2(1)	0.9(1)
${\sigma_{\mathrm{Au-Au}}}^2$ (10^{-2} Å^2)	—	0.78(2)	1.0(1)	1.06(8)	0.87(3)
${\sigma_{\mathrm{Au-Rh}}}^2$ (10^{-2} Å^2)	—	—	1.0(2)	2(1)	0.9(1)

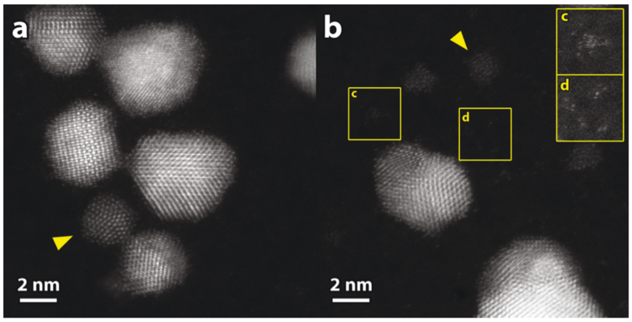

Fig. 6 HAADF-STEM micrographs of the (a) 0.5 : 0.5 and (b) 0.9 : 0.1 Rh/Au systems. The arrowheads indicate examples of small (≤2 nm), pure-Rh NPs. The insets (c and d) are regions of (b) that have been enlarged and increased in contrast to enhance the visibility of the (c) ultrasmall clusters and (d) non-associated atoms.

and intra-particle composition mapping of nanometer-sized particles (Fig. 7). This examination revealed highly heterogeneous, multimodal morphologies: larger (∼3–10 nm), core–shell-like Rh/Au NPs (Au@Rh); smaller (1–3 nm) unalloyed Rh-only NPs; and a Rh-rich background of sub-nm clusters and non-associated individual atoms (*e.g.*, Fig. 6b insets). Both the NP size and relative abundance of the particle type depended on the stoichiometry, and for the larger, mixed-metal particles, their morphology and composition varied with stoichiometry, as well. In the 0.5 : 0.5 system, the larger, mixed-metal particles consisted of Au-rich cores with Rh-rich shells, with overall compositions near the nominal stoichiometry. These shells were not always continuous, sometimes exhibiting a preferential attachment of the Rh to certain facets of the Au cores (*e.g.*, Fig. 7, white arrow). The integrated EDS signal from the non-NP portions of the maps was found to be Rh-rich (69–83 at% Rh), confirming that the ultrasmall clusters and non-associated atoms were predominately Rh. In the 0.9 : 0.1 system, the mixed-metal particles appeared more strongly phase segregated, approaching a more Janus particle-like arrangement. These particles were also significantly Au-enriched (37–71 at% Au). Correspondingly, the relative number of smaller Rh-only NPs was greater, and the background signal (ultrasmall clusters and non-associated atoms) was even richer in Rh (76–86 at%). These TEM results provided the necessary information to develop heterogeneous multi-particle models that agree significantly better with the EXAFS spectra (see below).

2.6. Quantitative structure model for Rh–Au NPs

Based on the heterogeneity in the NP size and composition observed with AC-S/TEM, we propose a model in which there are two different types of NPs present in the sample: (a) ultrasmall (<2 nm) particles of pure Rh and (b) larger (∼5 nm) NPs that contain both Rh and Au. Furthermore, we attempt to understand from the available EXAFS and microscopy data the structure of these larger particles in more detail.

The parameters of our model include the size of the large and small particles, their ratio in the sample, the elemental composition of the large particles, and the degree to which Au and Rh are segregated from each other and to the surface of the large NP. For comparison with the measured EXAFS data, the size of the particles is expressed in terms of the total coordination number of metal atoms in the large particles, $N_{\mathrm{M-M,L}}$ and the small particles, $N_{\mathrm{M-M,S}}$. In this notation, M indicates the total contribution from Au and Rh and L or S indicates the large or small particle. The fraction of metal atoms in the large particles is defined as X_{L}. Then, it is possible to calculate the average coordination numbers that would be measured from a population of both particles,

$$N_{\mathrm{Au-Au}} = \frac{S_{\mathrm{Au-Rh}} X_{\mathrm{Au,L}} S_{\mathrm{Au-surf}}}{X_{\mathrm{Au,L}} S_{\mathrm{Au-surf}} + 1 - X_{\mathrm{Au,L}}} N_{\mathrm{M-M,L}} \tag{1}$$

$$N_{\mathrm{Au-Rh}} = \frac{(1 - S_{\mathrm{Au-Rh}} X_{\mathrm{Au,L}}) S_{\mathrm{Au-surf}}}{X_{\mathrm{Au,L}} S_{\mathrm{Au-surf}} + 1 - X_{\mathrm{Au,L}}} N_{\mathrm{M-M,L}} \tag{2}$$

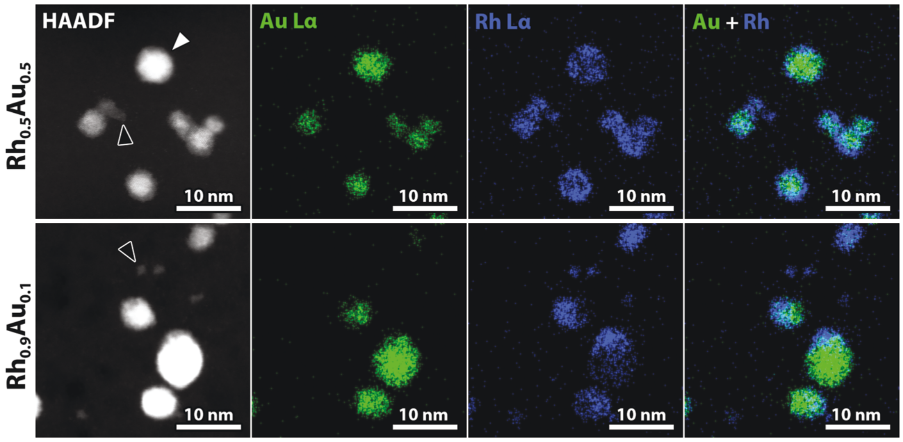

Fig. 7 Energy-dispersive X-ray spectroscopy (EDS) elemental maps of the (upper) 0.5 : 0.5 and (lower) 0.9 : 0.1 Rh/Au systems. The black arrowheads indicate the examples of small, pure-Rh NPs. The white arrowhead indicates a particle with preferential attachment of Rh to certain facets of the Au-rich core.

$$N_{\mathrm{Rh-Au}} = \frac{X_{\mathrm{L}}X_{\mathrm{Au,L}}}{(1-X_{\mathrm{L}}X_{\mathrm{Au,L}})}\frac{(1-S_{\mathrm{Au-Rh}}X_{\mathrm{Au,L}})S_{\mathrm{Au-surf}}}{(X_{\mathrm{Au,L}}S_{\mathrm{Au-surf}}+1-X_{\mathrm{Au,L}})} \times N_{\mathrm{M-M,L}} \tag{3}$$

$$N_{\mathrm{Rh-Rh}} = \frac{X_{\mathrm{L}}N_{\mathrm{M-M,L}}(1-X_{\mathrm{Au,L}}-S_{\mathrm{Au-surf}}X_{\mathrm{Au,L}}+S_{\mathrm{Au-Rh}}S_{\mathrm{Au-surf}}X_{\mathrm{Au,L}}^{2})}{(X_{\mathrm{Au,L}}S_{\mathrm{Au-surf}}+1-X_{\mathrm{Au,L}})(1-X_{\mathrm{L}}X_{\mathrm{Au,L}})} + \frac{(1-X_{\mathrm{L}})N_{\mathrm{M-M,S}}}{1-X_{\mathrm{L}}X_{\mathrm{Au,L}}}, \tag{4}$$

where $X_{\mathrm{Au,L}}$ is the elemental fraction of Au in the large particles, and

$$S_{\mathrm{Au-Rh}} = \frac{N_{\mathrm{Au-Au,L}}}{N_{\mathrm{Au-M,L}}}\frac{1}{X_{\mathrm{Au,L}}} \tag{5}$$

is a compositional segregation parameter, defined as the relative probability of Au–Au neighbors as compared to a random alloy where $S_{\mathrm{Au-Rh}} = 1$. The second segregation parameter,

$$S_{\mathrm{Au-surf}} = \frac{N_{\mathrm{Au-M,L}}}{N_{\mathrm{Rh-M,L}}}, \tag{6}$$

is the relative probability of Au–M bonds as compared with Rh–M bonds in the large NPs. $S_{\mathrm{Au-surf}} > 1$ indicates that Rh is favored on the surface of the large NPs and $S_{\mathrm{Au-surf}} < 1$ indicates that Rh is favored on the NP core. We can now solve these equations for the NP structural parameters (X_{L}, $X_{\mathrm{Au,L}}$, $N_{\mathrm{M-M,L}}$, and $N_{\mathrm{M-M,S}}$) as a function of the two segregation parameters, $S_{\mathrm{Au-Rh}}$ and $S_{\mathrm{Au-surf}}$, using coordination numbers from EXAFS ($N_{\mathrm{Au-Au}}$, $N_{\mathrm{Au-Rh}}$, $N_{\mathrm{Rh-Rh}}$, and $N_{\mathrm{Rh-Au}}$) and information on the particle sizes from S/TEM as the input.

The values of $N_{\mathrm{M-M,L}}$ and $N_{\mathrm{M-M,S}}$ as functions of the segregation parameters $S_{\mathrm{Au-Rh}}$ and $S_{\mathrm{Au-surf}}$ are shown in Fig. 8. For $\mathrm{Rh_{0.9}Au_{0.1}}$, certain values of $S_{\mathrm{Au-Rh}}$ and $S_{\mathrm{Au-surf}}$ allow for the presence of Rh–Au NPs with size *ca.* 3 nm and the presence of ultrasmall Rh NPs with sizes below 1 nm, which are observed in the size-distribution from STEM. The corresponding region in the ($S_{\mathrm{Au-Rh}}$, $S_{\mathrm{Au-surf}}$) parameter space is highlighted by the green lines in Fig. 8. These regions overlap for $S_{\mathrm{Au-Rh}}$ values between 3.5 and 5.5 and $S_{\mathrm{Au-surf}}$ values between 0.84 and 0.88. Hence, in this region, both EXAFS data and TEM data are in agreement for the $\mathrm{Rh_{0.9}Au_{0.1}}$ sample. The corresponding values for the structural parameters $N_{\mathrm{M-M,L}}$, $N_{\mathrm{M-M,S}}$, X_{L}, and $X_{\mathrm{Au,L}}$ are listed in Table 3. They indicate that about 60–80% of all atoms in the $\mathrm{Rh_{0.9}Au_{0.1}}$ sample are located within larger NPs (*ca.* 3 nm), while the remaining atoms reside in the pure Rh NPs with sizes below 1 nm. In the larger NPs, the Au concentration is only 10–20%. However, these Au atoms are concentrated in a few Au-rich regions indicated by $S_{\mathrm{Au-Rh}}$ values greater than 1. Smaller total coordination numbers for Au atoms than for Rh atoms in these larger NPs suggest that these Au-rich regions are located preferentially at the surface of larger NPs, although we note that there is a large uncertainty in the Au coordination numbers in this sample

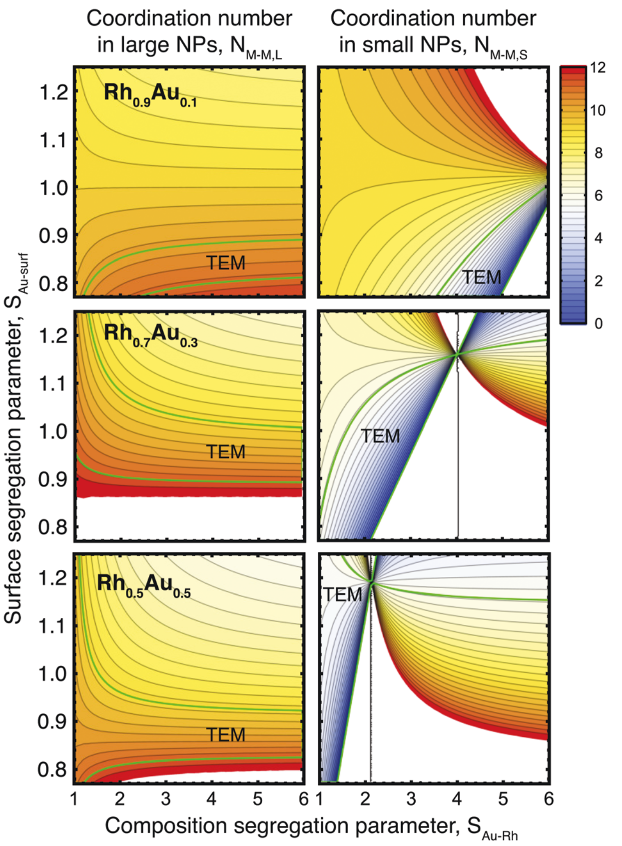

Fig. 8 Calculated coordination numbers, $N_{\mathrm{M-M,L}}$ and $N_{\mathrm{M-M,S}}$, as functions of the compositional $S_{\mathrm{Au-Rh}}$ and surface $S_{\mathrm{Au-surf}}$ segregation parameters. The regions between the green lines correspond to the size distributions of large (left) and small (right) particles observed from STEM.

($N_{\mathrm{Au-M}} = 9 \pm 2$), and that Au surface segregation is not observed with TEM.

A similar analysis for $\mathrm{Rh_{0.5}Au_{0.5}}$ and $\mathrm{Rh_{0.7}Au_{0.3}}$ is also shown in Fig. 8. Note that for $\mathrm{Rh_{0.7}Au_{0.3}}$, we do not have reliable information on the particle size distribution from STEM. Therefore, we assumed a similar broad particle size distribution as obtained for $\mathrm{Rh_{0.5}Au_{0.5}}$. In contrast to $\mathrm{Rh_{0.9}Au_{0.1}}$, one can see that the value of the compositional segregation parameter $S_{\mathrm{Au-Rh}}$ should be between 1 and 1.8 for $\mathrm{Rh_{0.5}Au_{0.5}}$ to ensure physically reasonable particle sizes and atom concentrations. This indicates some segregation of Au and Rh in $\mathrm{Rh_{0.5}Au_{0.5}}$ but less than that in the $\mathrm{Rh_{0.9}Au_{0.1}}$ sample.

For $\mathrm{Rh_{0.7}Au_{0.3}}$ (without using STEM information), the acceptable values for the segregation coefficient $S_{\mathrm{Au-Rh}}$ can vary broadly, from $S_{\mathrm{Au-Rh}} = 1$ (no segregation in larger particles) to higher values with increased segregation. Interestingly, the surface segregation coefficient $S_{\mathrm{Au-surf}}$ is always larger than 1, indicating that Au does not favor the surface of NPs. This conclusion can also be seen from the total Au coordination number $N_{\mathrm{Au-M,L}}$, which is equal to the bulk value of 12, indicating that Au is located predominantly below the NP surface. Furthermore, if we assume that the particle size distribution is similar to that in the $\mathrm{Rh_{0.5}Au_{0.5}}$ sample, we

Table 3 Average coordination numbers in the large Rh–Au NPs and ultrasmall Rh NPs ($N_{\mathrm{M-M,L}}$ and $N_{\mathrm{Rh-Rh,S}}$), relative concentration of Au atoms in the large NPs ($X_{\mathrm{Au,L}}$), the fraction of atoms within the large NPs (X_{L}), the compositional segregation parameter ($S_{\mathrm{Au-Rh}}$), and the surface segregation parameter ($S_{\mathrm{Au-surf}}$)

	Random alloy			Segregated		
	$Rh_{0.9}Au_{0.1}$	$Rh_{0.7}Au_{0.3}$	$Rh_{0.5}Au_{0.5}$	$Rh_{0.9}Au_{0.1}$	$Rh_{0.7}Au_{0.3}$	$Rh_{0.5}Au_{0.5}$
$N_{\mathrm{M-M,L}}$	9(1)	12(2)	10.3(4)	10.7(10)	10.2(7)	10(2)
$N_{\mathrm{M-M,S}}$	9.0(4)	6.0(4)	5.0(2)	0–7	0–6	0–5
$X_{\mathrm{Au,L}}$	0.76(6)	0.7(1)	0.85(2)	0.1–0.2	0.2–0.5	>0.5
X_{L}	0.16(6)	0.3(1)	0.47(7)	0.6–0.9	0.3–0.8	<0.8
$S_{\mathrm{Au-Rh}}$	1	1	1	3.8–5.6	1.3–3.0	1.0–1.7
$S_{\mathrm{Au-surf}}$	1	1	1	0.8–0.9	1.1–1.3	0.8–1.3

can improve the range of acceptable parameter values. Both green regions in Fig. 8 overlap in the $S_{\mathrm{Au-Rh}}$-range between *ca.* 1.3 and 3.3, which suggests that Rh and Au segregation within the large particles in the $Rh_{0.7}Au_{0.3}$ sample is more pronounced than in the $Rh_{0.5}Au_{0.5}$ sample (with $S_{\mathrm{Au-Rh}}$ values below 1.8), but smaller than in the $Rh_{0.9}Au_{0.1}$ sample (with $S_{\mathrm{Au-Rh}}$ values between 3.8 and 5.6). $S_{\mathrm{Au-surf}}$ values between 1.1 and 1.5 indicate that some Au had segregated toward the NP cores in the $Rh_{0.7}Au_{0.3}$ sample. The total Au concentration in the large RhAu particles $X_{\mathrm{Au,L}}$ is then between 0.2 and 0.5 (somewhat larger than in the $Rh_{0.9}Au_{0.1}$ sample, where the Au concentration is 0.1–0.2, but smaller than in the $Rh_{0.5}Au_{0.5}$ sample, where the Au concentration is above 0.5). Finally, the fraction of atoms in large NPs can vary in a broad range between 40 and 80%. Similar values were obtained for the other samples: for $Rh_{0.5}Au_{0.5}$ less than 80% of the atoms are within the large particles, while for $Rh_{0.9}Au_{0.1}$ there are between 60 and 80% of the atoms in the large particles.

2.7. Structure determination through atomistic simulation

TEM studies provide 2D projections of the morphologies and elemental distributions of RhAu NPs, while EXAFS analysis can give average values for local bonding information. However, both lack the ability to reconstruct NP structures with a full atomic resolution. To achieve this goal, we performed atomistic simulations of the EXAFS spectra of various proposed structures of RhAu NPs. The structure with the minimal difference in the experimental Rh K-edge and Au L_3-edge EXAFS spectra is considered as the representative atomic structure for the synthesized RhAuNPs. The method has been successfully applied previously to characterize the atomic structure of Au DENs[12,13] and Co oxides.[14] Briefly, to obtain the EXAFS spectra of atomistic models, we developed an empirical potential for the RhAu binary system of the modified embedded-atom method (MEAM) form. Monte Carlo (MC) simulations were performed to generate an ensemble of equilibrium structures from which FEFF6-lite[15] was used to calculate the corresponding EXAFS spectra.

The candidate models used for the structural screening were constructed as follows. First, a host Rh NP with a truncated-octahedral shape was selected. The diameter of the Rh NPs ranged from 2.5 nm (586 atoms) to 5.1 nm (4033 atoms) assuming an FCC lattice constant of 3.8 Å. Au grains were then added to the selected Rh NP host. The size of the Au grains ranged from one single Au atom, corresponding to a random alloy, to a Au grain having a radius of five nearest-neighbor distances (5 NN), containing 603 atoms. The Au grains of different sizes were randomly added to the Rh NP by replacing Rh atoms with Au to make a series of Rh/Au NPs with Au compositions ranging from 10 to 90%. In this way, atomic models of different compositions and degrees of phase segregation were constructed. Visualizations of Rh NPs and Au grains are shown in Fig. 9. There were 144 proposed Rh/Au structures in total. The difference between the simulated and experimental EXAFS spectra was evaluated as $\int_{r_{\min}}^{r_{\max}} \left| \mathrm{FT_{mag}} k^2 \chi_{\mathrm{sim}} - \mathrm{FT_{mag}} k^2 \chi_{\mathrm{exp}} \right| \mathrm{d}r$, where $\mathrm{FT_{mag}}$ is the magnitude of the complex Fourier transformation of the EXAFS spectra. This integral was evaluated for both the Rh K-edge and Au L_3-edge, and a sum of both edges was used to calculate the difference between the experiment and the simulated model.

Before discussing the results, it is helpful to first get a sense of how alloying influences the EXAFS spectra of the Au L_3 and the Rh K-edge. To do this, we built FCC crystals for Rh and Au with their corresponding lattice constants. One atom in the Rh (Au) crystal was then changed to Au (Rh). The crys-

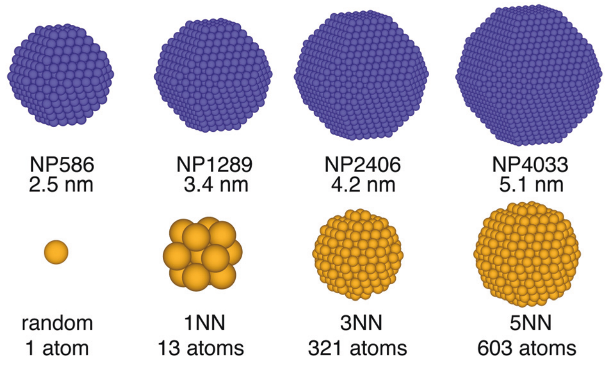

Fig. 9 Atomic models used for structural screening. NPs were constructed using a Rh host in the size range from 2.5 to 5.1 nm. To these particles, Au regions were added (replacing Rh atoms) with grain sizes ranging from a single Au atom to the largest grains considered with 5 Au nearest neighbor shells (5 NN) containing a total of 603 atoms.

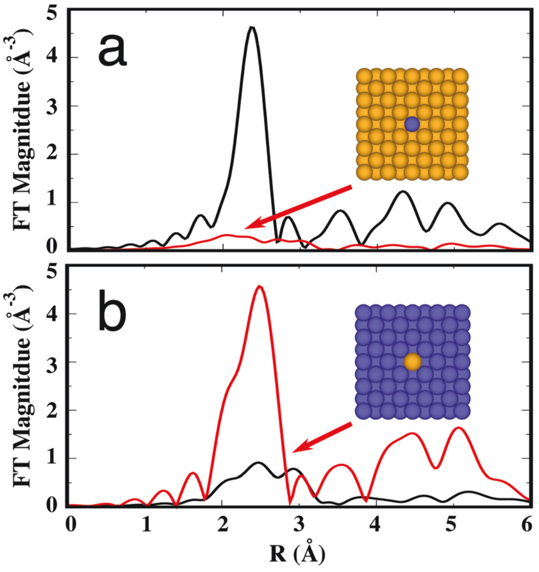

Fig. 10 Alloying effect on the EXAFS spectra of (a) Rh K- and (b) Au L_3-edges. The black curves are for the EXAFS spectra of (a) Rh bulk and (b) Au bulk. The red curves are for the EXAFS spectra of (a) a single Rh atom in bulk Au and (b) a single Au atom in bulk Rh.

tals with the impurities were equilibrated at 298 K and the EXAFS spectra of the impurities were evaluated. In Fig. 10(a), it can be seen that the EXAFS spectrum of the Au impurity in a Rh crystal has a significantly higher magnitude than the spectrum of a Au foil. The enhanced signal from the Au impurity can be attributed to the decreased dynamical Debye–Waller factor in the stiff Rh matrix as compared to bulk Au. Quantitatively, the Debye–Waller factor decreases from 0.84 to 0.29×10^{-2} Å^2. Similarly, the EXAFS spectrum of the Rh impurity in a Au crystal has a low magnitude compared to the Rh foil due to an increased Debye–Waller factor from 0.38 to 0.90×10^{-2} Å^2. These and other fit parameters are given in Table S3.†

Our initial structural screening employed single NP models of nominal compositions to find candidate atomic structures consistent with the $Rh_{0.9}Au_{0.1}$, $Rh_{0.7}Au_{0.3}$, and $Rh_{0.5}Au_{0.5}$ samples. The underlying assumption of the single NP model is that the synthesized RhAu NPs are structurally homogeneous and can be accurately represented by a single NP. Since the composition of the proposed RhAu NPs was fixed to the nominal compositions, the variables are the size and degree of compositional segregation of the NPs. In order to identify the most significant differences between the single-particle model and the experimental EXAFS, we fit the simulated EXAFS from the single-particle model and looked to see which parameters varied most significantly as compared to the experiment. The fitted EXAFS spectra along with the simulated spectra are shown in Fig. S6† and the extracted structural parameters are summarized in Table S5.†

The screening results are shown in Fig. 11. For the $Rh_{0.9}Au_{0.1}$ sample, the best model is a pure Rh NP of size 2.5 nm with 10% of Au in a segregated grain about 3 NN (321 atoms) in size. The Rh K-edge for this model matched the high magnitude of the Rh K-edge in the experimental EXAFS spectrum, indicating a Rh NP with little Au alloying. However, the predicted Rh-K edge was shifted to lower *R* as compared to the experiment. This could be an indication of more Au atoms in the NP as a greater number of Rh–Au bonds would increase the average Rh–M bond length longer. For the Au L_3-edge, the match between the experiment and simulation is not as good as for the Rh K-edge. The magnitude of the Au L_3-edge spectrum between 2–3 Å is higher than in the experiment. This discrepancy could be due to the overestimation of the portion of

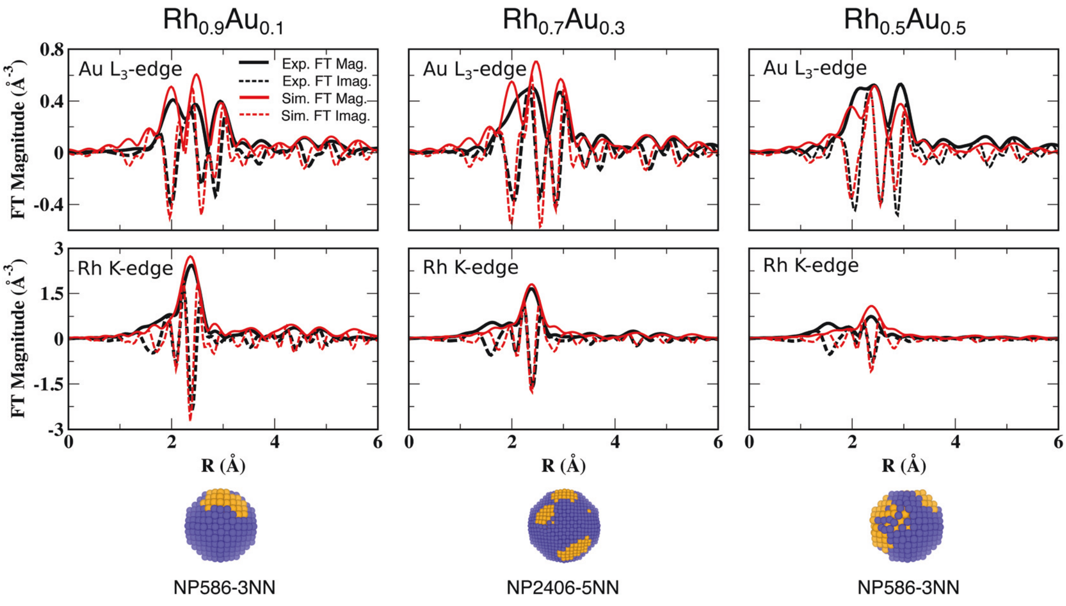

Fig. 11 Comparison of the experimental and simulated Au L_3-edge and Rh K-edge EXAFS spectra. The best-fit single-NP models employed to simulate EXAFS spectra are shown for each case. Blue spheres represent Rh atoms; gold are Au.

Au–Rh bonds out of the total Au–M bonds since Au–Rh bonding would cause the magnitude of the Au L_3-edge spectrum to be higher as shown in Fig. 10. The fitted structural parameters (shown in Table S5†) also suggest that $N_{\mathrm{Rh-Rh}}$ and $N_{\mathrm{Au-Rh}}$ need to be decreased, while $N_{\mathrm{Au-Au}}$ needs to be increased to better match the experimental data. Considering the discrepancies for both the Rh K-edge and Au L_3-edge spectra in the $Rh_{0.9}Au_{0.1}$ sample, the RhAu NPs should have more Au atoms present in larger Au grains. These discrepancies can be resolved by including the small pure Rh NPs observed by STEM, so that the larger NPs can be enriched with Au.

For the $Rh_{0.7}Au_{0.3}$ sample, the predicted structure is a 4.2 nm NP with 5 NN Au grains. A similar discrepancy in the Au L_3-edge spectrum is also present in the $Rh_{0.9}Au_{0.1}$ sample. In contrast, for the $Rh_{0.5}Au_{0.5}$ sample the predicted structure seems to underestimate the percentage of Au–Rh bonds since the simulated Au L_3-edge has lower magnitude than the experiment. For this reason, the real RhAu NPs should have more alloying. The single particle model for the $Rh_{0.5}Au_{0.5}$ sample also overestimates the magnitude of the Rh K-edge spectrum, which could also be improved by the inclusion of small pure Rh clusters. Sizable discrepancies can be observed (Table S5†), especially for the Rh–Rh and Rh–Au coordination numbers. This is consistent with the fact that the best single-particle model is not able to capture the low Rh coordination numbers that are observed in the EXAFS data.

Including the ultrasmall Rh clusters yields a structural model that better reproduces the experimental EXAFS data. Specifically, we choose a two-particle model with (i) a fraction of small Rh_{38} clusters and (ii) larger RhAu NPs constructed in the same way as for the single-NP model. The overall composition is constrained to the nominal composition during fitting. The Rh_{38} structure is disordered as predicted by our MEAM potential and MC simulations to find stable structures. The average coordination number for the Rh_{38} ($N_{\mathrm{Rh-Rh,S}}$) is about 6.3. The fitting results for this two-particle model are shown in Fig. 12. It can be seen that the overall agreement with the experiment is improved for all three samples compared to the single-particle model. The Rh K-edge spectra match very well (Fig. 12) except for the peaks at short distances corresponding to oxidized Rh, which cannot be captured by our model. The remaining differences between the simulated and experimental Au L_3-edge spectra are mainly found in the second peak, at about 2.5 Å. We do not fully understand this discrepancy. One possible reason is that there is more heterogeneity in the experimental samples than is captured in our two-particle model.

As with the single-particle model, we fit the simulated EXAFS spectra to extract the structural parameters for a quantitative comparison with the experimental values. The simulated EXAFS spectra and its fit are listed in Fig. S7.† The resulting structural parameters are shown in Table S6.† The predicted larger RhAu NP in the 0.9 : 0.1 sample contains 20% Au, *i.e.* $X_{\mathrm{Au,L}} = 0.2$ and the degree of compositional segregation $S_{\mathrm{Au-Rh}} = 3.3$. The fraction of atoms in the larger NP is $X_{\mathrm{L}} = 0.51$, and the average coordination, $N_{\mathrm{M-M,L}} = 10.1$. For $Rh_{0.7}Au_{0.3}$, $X_{\mathrm{Au,L}} = 0.4$, $X_{\mathrm{L}} = 0.75$, $S_{\mathrm{Au-Rh}} = 2.0$, and $N_{\mathrm{M-M,L}} = 9.7$. For $Rh_{0.5}Au_{0.5}$, $X_{\mathrm{Au,L}} = 0.7$, $X_{\mathrm{L}} = 0.72$, $S_{\mathrm{Au-Rh}} = 1.3$, and $N_{\mathrm{M-M,L}} = 10.0$. These parameters are in agreement with the prediction made by the analytic model presented above, while the atomistic simulations provide more details on the actual elemental distribution. For all samples, the segregation of Rh and Au is clear from the large Au grain sizes in the optimal structures for all samples.

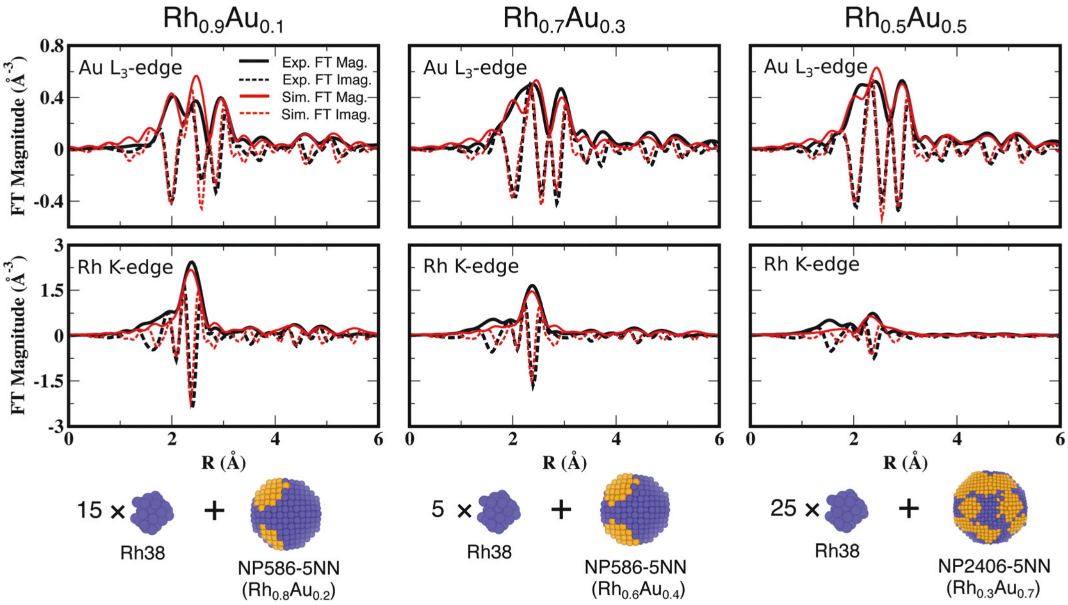

Fig. 12 Comparison of the experimental and simulated Au L_3-edge and Rh K-edge EXAFS spectra. The best-fit bimodal models employed to simulate the EXAFS spectra are shown for each case.

In the above heterogeneous model, Rh38 was selected to represent the small Rh NPs because it gave the best overall fit simultaneously to all the samples. As a sensitivity test for the choice of Rh38, we performed the same fit using Rh201 and Rh13. The results are shown in Fig. S8 and S9,† respectively. It can be seen that the fit for the Au L_3-edge spectrum of the $Rh_{0.5}Au_{0.5}$ sample is less accurate when Rh201 is employed. When Rh13 is employed, the fits for the $Rh_{0.9}Au_{0.1}$ and $Rh_{0.7}Au_{0.3}$ samples degraded especially on the Rh K-edge.

3. Conclusions

We have employed various structural characterization techniques including S/TEM, EXAFS, and atomistic simulation to determine the atomic structures of RhAu NPs synthesized by the microwave-assisted method. Initially, using standard experimental TEM and XRD measurements, we were misled into believing that our RhAu NPs were relatively uniform random-alloys. EXAFS data of these particles, combined with theoretical modeling, indicated that no single-particle model was consistent with the experimental data. With the aid of high-resolution (S)TEM, the synthesized RhAu NPs of different compositions are found to have a bimodal distribution, in which there exist ultrasmall pure Rh NPs and larger RhAu alloy NPs. An EXAFS analysis, based upon a two-particle model with sizes from (S)TEM, provides quantitative structural information including coordination numbers of pure Rh and RhAu NPs, compositions of RhAu NPs, and degrees of segregation in the RhAu NPs. Finally, atomistic simulations were used to fit the experimental EXAFS spectrum. The best-fit atomic structures, again using a two-particle model, are in agreement with the results obtained by EXAFS analysis. In summary, we demonstrated that this range of structural characterization techniques combined with modeling is capable of reconstructing the atomic structures of heterogeneous NPs more accurately and completely than either technique alone.

4. Experimental and computational methods

4.1. Synthesis

Metal salts (0.1 mmol total) were co-dissolved in 5 mL of ethylene glycol (EG) using sonication and vortexing in a 20 mL glass scintillation vial. Separately, polyvinylpyrrolidone (PVP) (222 mg, 0.2 mmol on a monomer basis) and $NaBH_4$ (5.6 eqv. based on the $HAuCl_4{\cdot}3H_2O$ concentration) were weighed and transferred using 15 mL of EG to a 50 mL single neck round bottom (RB) flask. $HAuCl_4{\cdot}3H_2O$ (49%, Strem), $RhCl_3{\cdot}xH_2O$ (38–41%, Strem), PVP (⟨M.W.⟩ = 58 000, Alfa Aesar), and EG (Certified, Fisher) were used without further purification. Thereafter, a reflux condenser was connected to the RB flask and the whole apparatus was placed inside the microwave cavity. A variable power method was used to ramp the temperature inside the microwave cavity to 150 °C with the reaction mixture stirred continuously. The pre-mixed metal salt solution ($RhCl_3{\cdot}xH_2O$ + $HAuCl_4{\cdot}3H_2O$) in EG was then added to the PVP and maintained at 150 °C using a dual-programmable syringe pump at a rate of 100–150 mL h^{-1} (2–3 mmol h^{-1}). A MARS 5 microwave system (CEM Corp.) operating with a fiber-optic temperature feedback control (RTP-300+, ±0.1 °C) and a maximum controllable power of up to 1600 W was used in all the reactions. The reaction mixture was maintained at 150 °C for 30 minutes after which the reaction was quenched using an ice-water bath. The NPs were purified by selective precipitation after addition of 70 mL acetone followed by vortexing and ultracentrifugation at 5500 RPM for 5 min. A second cycle was carried out using 15 mL ethanol for dissolution and 75 mL hexanes for precipitation followed by ultracentrifugation (5500 RPM, 5 min). The resulting NPs were stored as a solid-polymer film under ambient conditions using 50 mL poly-propylene tubes.

4.2. Characterization

Powder X-ray diffraction studies were carried out using a Spider diffractometer (Rigaku Corporation) operated at 40 kV and 40 mA using a Cu Kα source (λ = 1.5418 Å).

Transmission electron microscopy samples were prepared by dispersing the NP-PVP composite in ethanol followed by sonication and vortexing in order to completely dissolve the composite. The resulting solution was drop cast onto a support of a 200-mesh copper Formvar grid (Ted Pella Inc.) and dried in air. Low-resolution transmission electron microscopy (TEM) was performed on an FEI Tecnai Transmission Electron Microscope. Size measurements and analysis of the NPs were performed using ImageJ software. To obtain the mean diameter and standard deviation of NPs, a minimum of 250 manual measurements were carried out for each sample using ImageJ. High resolution TEM images, high-angle annular dark field scanning transmission electron microscopy (HAADF-STEM) images, and EDS spectra were obtained using a JEOL 2010F TEM instrument equipped with an Oxford EDS detector. The operating voltage was 200 KeV and the point to point resolution was 0.19 nm.

Trace metal grade hydrochloric acid (HCl, JT Baker, 36.5–38.0%) and nitric acid (JT Baker, 69.0–70.0%) were used to perform ICP analysis. For ICP-OES analysis, Rh_xAu_{1-x} alloy NPs were thermally digested using EasyPrep Plus Vessels under microwave heating. Approximately, 2 mg of PVP-NP composites were added to ≈10 ml of aqua regia, prepared using trace metal acids, with precise weight determination. After attaining the desired temperature of 150 °C (1st stage ramp: a temperature increase from 25 °C to 100 °C in 60 min; 2nd stage ramp: a temperature increase from 100 to 150 °C in 45 min), digestion was continued at 150 °C for 3 more hours following which the reaction mixtures were cooled down to room temperature. The solutions obtained thus were diluted using 2% trace metal grade HCl before being analyzed.

4.3. EXAFS measurement and data fitting

The synthesized RhAu NPs with nominal Rh : Au compositions: 90 : 10, 70 : 30, and 50 : 50 were probed with the EXAFS method. Besides, a sample of pure Rh NPs was also studied. All the investigated samples were ground with BN and pressed into pellets with a diameter of 13 mm. For all samples, we carried out measurements at room temperature in air. Measurements have been carried out in transmission and fluorescence modes. We analyzed the results obtained in transmission mode since the quality of the obtained spectra was higher. The radiation from the storage ring was monochromatized by using a Si(220) double-crystal monochromator. For the Rh K-edge, the monochromator was fully tuned, while for measurements at the Au L_3-edge, 20% detuning was used. The intensity of X-rays before and after the sample was measured by two ionization chambers. For measurements at the Rh K-edge, the I_0 detector was filled with pure argon, while for measurements at the Au L_3-edge a mixture of 10% Ar and 90% N_2 was used. For I_1 detection, an argon and krypton 1 : 1 mixture was used.

Here, we analyzed Rh K-edge and Au L_3-edge EXAFS in $Rh_{0.7}Au_{0.3}$ and $Rh_{0.5}Au_{0.5}$NPs. Conventional least-square fitting to theoretical standards, as implemented in the FEFFIT code,[15] was applied, but in this case data from both absorption edges were fitted simultaneously to obtain a structure model, consistent with all available experimental information. We analyze the contributions from the first coordination shell only. For NPs, the fitted variables were coordination numbers N, average distances $\langle R\rangle$, and MSRD factors σ^2 for Rh–Rh, Rh–Au, Au–Au, and Au–Rh pairs. We constrained $\langle R\rangle$ and σ^2 for the Rh–Au pair to be equal to $\langle R\rangle$ and σ^2 for the Au–Rh pair. Initially, we did not apply any constraints on coordination numbers, but it resulted in very large uncertainties for structural parameters. Hence, we set $N_{\mathrm{AuRh}} = \frac{0.72}{0.28}N_{\mathrm{RhAu}}$ for $Rh_{0.7}Au_{0.3}$NPs and $N_{\mathrm{AuRh}} = \frac{0.46}{0.54}N_{\mathrm{RhAu}}$ for $Rh_{0.5}Au_{0.5}$, where $\frac{0.72}{0.28}$ and $\frac{0.46}{0.54}$ terms reflect the ratio of Rh and Au atoms in the investigated NPs, calculated from the values of absorption edges as shown in Table 1. Theoretical phases and amplitudes were obtained in self-consistent *ab initio* calculations with the FEFF8.5 code[16] for the bulk material. The complex exchange–correlation Hedin–Lundqvist potential and default values of muffin-tin radii as provided within the FEFF8.5 code were employed. For the Rh K-edge, data fitting was carried out in the range from $R_{\min}$ = 2.1 Å up to $R_{\max}$ = 3.4 Å. Fourier transform was carried out in the k range from 3.0–14.0 $Å^{-1}$. For the Au L_3-edge, the values ΔE_0 = 0.1(4) eV and $S_0{}^2$ = 0.89(5) were obtained from the fit of Au foil EXAFS data. For the Au L_3-edge, fitting was carried out in the range from $R_{\min}$ = 1.7 Å up to $R_{\max}$ = 3.6 Å. Fourier transform was carried out in the k range from 3.0–10.0 $Å^{-1}$.

4.4. Density functional theory

Density functional theory (DFT) calculations were carried out using the Vienna *ab initio* simulation package.[17,18] All calculations were spin-polarized. Core electrons were described with the projector augmented-wave (PAW) method.[19,20] The Kohn–Sham wave functions for the valence electrons were expanded in a plane-wave basis set with an energy cutoff of 300 eV. The exchange–correlation energy was treated within the framework of the generalized gradient approximation. Specifically, PBEsol[21] was used, which is a modified form of the Perdew–Burke–Ernzerhof (PBE) functional designing to improve lattice parameters and surface energies in solids. A single Γ-point was sufficient for integration of the reciprocal space due to the finite nature of the NPs. A unit cell of 5 × 5 × 5 was used to model the Au bulk and simulate the EXAFS spectrum for Au foil. A k-point mesh of 2 × 2 × 2 was used for this periodic model.

4.5. EXAFS simulation

We attempt to reconstruct 3D atomic structures of the synthesized Rh–Au NPs with atomistic simulations. Specifically, we propose a broad variety of atomic models for Rh–Au NPs. The goodness of fit for the proposed structures to the structures of real NPs is examined by comparing the simulated EXAFS spectra of the proposed models with the experimental EXAFS spectra. Models with the EXAFS spectra in close resemblance to the experimental EXAFS spectra are considered to be good representative structures for the synthesized Rh–Au NPs.

To simulate the EXAFS spectra of atomic models, an ensemble of equilibrium structures at finite temperatures is needed. In this work, Monte Carlo (MC) simulations are employed to sample the equilibrium structures. And, we developed empirical potentials in the framework of the modified embedded-atom method (MEAM)[22,23] to describe atomic interactions in the Rh–Au system.

In the MEAM, the total energy of a metallic system is calculated as

$$E = \sum_i [F(\bar{\rho}_i) + \frac{1}{2}\sum_{j\neq i}\Phi(R_{ij})]. \tag{7}$$

In the equation, the first term is the embedding energy of atom i which is embedded into the electron density $\bar{\rho}_i$ and the second term is the core–core pair interaction between atoms i and j separated by a distance R_{ij}. Here, $\bar{\rho}_i$ is the background electron density at the center of atom i obtained by superposing the electronic densities from its surrounding atoms. To compute $\bar{\rho}_i$, we chose an FCC lattice as the reference structure of pure Rh–Rh and Au–Au potentials and the Rh_3Au crystal of $L1_2$ was used as the reference structure for Rh–Au cross-potentials. The detailed formula of the MEAM potentials could be found in ref. 22, 24, 25, and 26.

The parameters for the developed Rh–Au MEAM potentials are given in Tables S1 and S2.† The employed MEAM potentials for pure Rh and Au metals were similar to those published in ref. 22, with some renormalized scaling factors in the atomic charge densities.[24] Besides, the parameters of pure Rh and Au metals are tuned to reproduce the experimental EXAFS spectra of Rh and Au foils. The parameters of cross-potential describing Rh–Au interactions are optimized based on our DFT results for the lattice constant, the bulk modulus, and the heat of formation of the Rh_3Au $L1_2$ crystal.

The MC simulation method employed in this work was implemented based on the Metropolis algorithm,[27] in which successive configurations were generated in proportion to the probabilities of a configuration occurring in the equilibrium ensemble. Starting from a given atomistic structure of the alloy system, we continuously tried out the configuration transformations of the system to reach the thermodynamically equilibrium ensembles. At each MC step, the energy difference ΔE associated with a configuration change of the system was evaluated using our developed MEAM potentials. If $\Delta E < 0$ (energy-decreasing process), the new configuration would always be retained, while if $\Delta E > 0$ (energy-increasing process), the new configuration would be accepted with the probability $\exp(-\Delta E/k_BT)$. Here, k_B is the Boltzmann constant and T is the temperature. We modeled the vibrational processes in the RhAu systems in this work through imposing displacements (in random directions) to randomly selected atoms as a type of configuration transformation in the MC simulations. For bulk systems, the volume of the simulation cell is allowed to change in response to the external pressure set to 1 bar. To simulate the EXAFS spectrum, we feed 200 snapshots of the sampled equilibrium structures by MC simulations to the FEFF6-lite program,[15] which is *ab initio* software capable of calculating the scattering properties of photo-excited electrons out of given atomic structures.

Using the above methods, we can well reproduce the experimental EXAFS spectra for Au and Rh foils as shown in Fig. S3(a) and (b),† respectively. Furthermore, the developed Rh–Au potentials can also well reproduce the simulated EXAFS spectra of Au L_3 and Rh K-edges of truncated-octahedral pure Au and Rh NP201 obtained with DFT as shown in Fig. S3(c) and (d),† respectively. We further tested the capability of the Rh–Au potentials by comparing the simulated EXAFS of Au L_3 and Rh K-edges of a $Rh_{0.75}Au_{0.25}$ random alloyed NP model with 201 atoms by the MEAM with the results obtained with DFT. The comparison is shown in Fig. S4.† For all the comparisons of EAXFS spectra, we quantify the comparison by extracting the structural parameters *via* fitting to the EXAFS spectra. The resulted structural parameters are shown in Tables S3 and S4.† Overall, the developed MEAM potentials can well reproduce the experimental EXAFS spectra and DFT-generated EXAFS spectra. The developed Rh–Au potentials can also make reliable predictions on the thermodynamics of RhAu alloys. As shown in Fig. S5,† we calculated the formation energies of RhAu NP model with 140 atoms of different elemental distributions with both DFT and MEAM. It can be seen that the results of MEAM potentials are in good agreement with the DFT results.

Conflicts of interest

There are no conflicts to declare.

Acknowledgements

Funding for this work was provided by the National Science Foundation under grants CHE-1534177 (G. H. and R. M. C.), CHE-1807847 (S. M. H. and G. H.), CHE-1534630 (J. C. Y.), and CHE-1534184 (A. I. F.). We also appreciate the support from the Welch Foundation (F-0032, F-1738, and F-1841). The authors acknowledge the facilities support provided at the Synchrotron Catalysis Consortium (U.S. DOE Grant No. DE-SC0012335). This research made use of resources from the Center for Functional Nanomaterials, which is a U.S. DOE Office of Science Facility, at Brookhaven National Laboratory under Contract No. DE-SC0012704. Additional exploratory microscopy was also performed at the National Center for Electron Microscopy in the Molecular Foundry, which is supported by the Office of Science, Office of Basic Energy Sciences, of the U.S. Department of Energy under Contract No. DE-AC02-05CH11231. Computational resources were provided by the National Research Scientific Computing Center and the Texas Advanced Computing Center.

References

1 S. T. Hunt, M. Milina, A. C. Alba-Rubio, C. H. Hendon, J. A. Dumesic and Y. Román-Leshkov, *Science*, 2016, **352**, 974–978.
2 A. S. Lapp, Z. Duan, N. Marcella, L. Luo, A. Genc, J. Ringnalda, A. I. Frenkel, G. Henkelman and R. M. Crooks, *J. Am. Chem. Soc.*, 2018, **140**, 6249–6259.
3 H. Li, L. Luo, P. Kunal, C. Bonifacio, Z. Duan, J. Yang, S. Humphrey, R. Crooks and G. Henkelman, *J. Phys. Chem. C*, 2018, **122**, 2712–2716.
4 G. W. Piburn, H. Li, P. Kunal, G. Henkelman and S. M. Humphrey, *ChemCatChem*, 2018, **10**, 329–333.
5 L. Luo, Z. Duan, H. Li, J. Kim, G. Henkelman and R. Crooks, *J. Am. Chem. Soc.*, 2017, **139**, 5538–5546.
6 S. Seraj, P. Kunal, H. Li, G. Henkelman, S. M. Humphrey and C. Werth, *ACS Catal.*, 2017, **7**, 3268–3276.
7 S. García, L. Zhang, G. W. Piburn, G. Henkelman and S. M. Humphrey, *ACS Nano*, 2014, **8**, 11512–11521.
8 L. Piccolo, Z. Y. Li, I. Demiroglu, F. Moyon, Z. Konuspayeva, G. Berhault, P. Afanasiev, W. Lefebvre, J. Yuan and R. L. Johnston, *Sci. Rep.*, 2016, **8**, 35226.
9 Y. Li, D. Zakharov, S. Zhao, R. Tappero, U. Jung, A. Elsen, P. Baumann, R. Nuzzo, E. Stach and A. Frenkel, *Nat. Commun.*, 2015, **6**, 7583.
10 A. I. Frenkel, *Chem. Soc. Rev.*, 2012, **41**, 8163–8178.
11 A. I. Frenkel, S. Nemzer, I. Pister, L. Soussan, T. Harris, Y. Sun and M. H. Rafailovich, *J. Chem. Phys.*, 2005, **123**, 184701.
12 D. F. Yancey, S. T. Chill, L. Zhang, A. I. Frenkel, G. Henkelman and R. M. Crooks, *Chem. Sci.*, 2013, **4**, 2912–2921.
13 Z. Duan, Y. Li, J. Timoshenko, S. T. Chill, R. M. Anderson, D. F. Yancey, A. I. Frenkel, R. M. Crooks and G. Henkelman, *Catal. Sci. Technol.*, 2016, **6**, 6879–6885.

14 Z. Chen, Z. Duan, Z. Wang, X. Liu, L. Gu, F. Zhang, M. Dupuis and C. Li, *ChemCatChem*, 2017, **9**, 3641–3645.

15 S. I. Zabinsky, J. J. Rehr, A. Ankudinov, R. C. Albers and M. J. Eller, *Phys. Rev. B: Condens. Matter Mater. Phys.B*, 1995, **52**, 2995–3009.

16 J. J. Rehr, J. J. Kas, F. D. Vila, M. P. Prange and K. Jorissen, *Phys. Chem. Chem. Phys.*, 2010, **12**, 5503–5513.

17 G. Kresse and J. Furthmüller, *Comput. Mater. Sci.*, 1996, **6**, 15–50.

18 G. Kresse and J. Furthmüller, *Phys. Rev. B: Condens. Matter Mater. Phys.*, 1996, **54**, 11169.

19 P. E. Blöchl, *Phys. Rev. B: Condens. Matter Mater. Phys.*, 1994, **50**, 17953.

20 G. Kresse and D. Joubert, *Phys. Rev. B: Condens. Matter Mater. Phys.*, 1999, **59**, 1758–1775.

21 J. P. Perdew, A. Ruzsinszky, G. I. Csonka, O. A. Vydrov, G. E. Scuseria, L. A. Constantin, X. Zhou and K. Burke, *Phys. Rev. Lett.*, 2008, **100**, 136406.

22 M. I. Baskes, *Phys. Rev. B: Condens. Matter Mater. Phys.*, 1992, **46**, 2727–2742.

23 M. I. Baskes and R. A. Johnson, *Model. Simul. Mater. Sci. Eng.*, 1994, **2**, 147.

24 G. Wang, M. A. V. Hove, P. N. Ross and M. I. Baskes, *J. Chem. Phys.*, 2004, **121**, 5410–5422.

25 M. I. Baskes, J. E. Angelo and C. L. Bisson, *Model. Simul. Mater. Sci. Eng.*, 1994, **2**, 505.

26 M. Baskes, *Mater. Chem. Phys.*, 1997, **50**, 152–158.

27 N. Metropolis, A. W. Rosenbluth, M. N. Rosenbluth, A. H. Teller and E. Teller, *J. Chem. Phys.*, 1953, **21**, 1087–1092.